SAKATA, M. & TAKATA, M. (1994). *MEND*. Nagoya Univ., Japan.
SATAKA, M., UNO, T., TAKATA, M. & HOWARD, C. J. (1993). *J. Appl. Cryst.* **26**, 159–165.
SEYMOUR, R. S. & PRYOR, A. W. (1970). *Acta Cryst.* B**26**, 1487–1491.
SMIT, J. G., DACHS, H. & LECHNER, R. E. (1979). *Solid State Commun.* **29**, 219–223.
ZHELUDEV, A., PAPOULAR, R. J., RESSOUCHE, E. & SCHWEIZER, J. (1995). *Acta Cryst,* A**51**, 450–455.

Acta Cryst. (1995). A**51**, 746–753

High-Q-Resolution X-ray Diffraction of Ordered Fe–Al Single Crystals

BY F. BLEY, F. LIVET, J. C. LEROUX AND J. P. SIMON
LTPCM (URA CNRS 29), ENSEEG-INPG, BP 75, 38402 Saint Martin d'Hères CEDEX, France

D. ABERNATHY, J. ALS-NIELSEN,* G. GRUEBEL AND G. VIGNAUD
European Synchrotron Radiation Facility, BP 220, 38043 Grenoble, France

G. DOLINO AND J. F. LEGRAND
Laboratoire de Spectrométrie Physique (URA CNRS 08), UJF BP 87, 38402 Saint Martin d'Hères CEDEX, France

D. CAMEL AND N. MENGUY†
Centre d'Etudes Nucléaires de Grenoble, 38041 Grenoble, France

AND M. PAPOULAR
Centre de Recherches sur les Très Basses Températures, CNRS, 38042 Grenoble, France

(*Received* 15 *February* 1995; *accepted* 22 *May* 1995)

Abstract

The use of synchrotron radiation in the study of ordering transitions is presented. The peak-profile measurements can be carried out with a resolution one order of magnitude better than with classical sources in all directions of the reciprocal lattice. In the case of Fe–Al alloys, the small-angle scattering techniques can be transposed in the vicinity of a Bragg superstructure peak, which provides information on the antiphase configuration of the ordered alloys. Moreover, the high brilliance of the undulator of the ESRF ID10 beamline enables coherent scattering experiments. The conditions necessary to record holograms from an inhomogeneous sample are discussed and some results are presented.

I. Introduction

The transitions occurring in $Fe_{(1-c)}Al_c$ alloys, $0.23 < c < 0.3$, have been extensively studied (Taylor & Jones, 1958; Morgand, Mouturat & Sainfort, 1968; Okamoto & Beck, 1971; Rimlinger, 1971; Swann, Duff & Fisher, 1972; Oki, Hasaka & Eguchi, 1973; Allen & Cahn, 1975, 1976, 1979; Köster & Gödecke, 1980; Kubaschewski, 1982; Anthony & Fultz, 1989; Inden & Pepperhoff, 1990; Park, Stephenson, Ludwig & Allen, 1992). At high temperatures, this system is in the A_2 phase, of b.c.c. structure, with a cubic cell of size a. With decreasing temperature, successively appear the B_2 phase of *sc* (CsCl) structure and the $D0_3$ phase, of f.c.c. stucture, with a doubled unit-cell parameter ($2a$).

In the units of the cubic cell (parameter a) of the A_2 phase, three types of Bragg peaks (hkl) can be distinguished, which are used to characterize the ordering:

$h + k + l = 2n$, h, k, l integers: fundamental peaks present in the three phases;

$h + k + l = 2n + 1$, h, k, l integers: superstructure peaks corresponding to both ordered phases;

$2h$, $2k$, $2l$ odd: characteristic of the $D0_3$ phase.

The careful study of the profile of the superstructure peaks provides information on the size and distribution of the domains of the various phases (Warren, 1969; Cheary & Grimes, 1972).

The transitions described here are essentially of second-order type, except close to the 24 at.% composition, where the convergence of the two transition lines and of the magnetic order leads to a complex phase diagram. Here, single crystals are used so that only the metastable coherent phase diagram has to be considered (Allen & Cahn, 1975).

* Present address: Risø National Laboratory, Roskilde, Denmark.
† Present address: Laboratoire MATOP, Université Saint-Jérôme, Case 151, 13397 Marseille CEDEX 20, France.

We have studied the increase of the domain size of the two ordering structures for various annealing times of samples quenched from the disordered state.

It will be shown that here the critical fluctuations are small. The kinetics of ordering of such alloys correspond to the antiphase surface reduction and to the increase of the characteristic length L of the ordered domains.

Theoretical arguments and experimental evidence (English, 1966) give a $t^{1/2}$ increase of L. This is mainly due to the formal equivalence of this evolution with the model A of the dynamics of the phase transitions (Hohenberg & Halperin, 1977). In this model, with a non-conserved order parameter, no long-range transport is necessary for the increase of L.

In this paper, we report very precise measurements using X-ray synchrotron radiation. We first discuss the high resolution in the reciprocal space (the q space), which can be achieved with a high-brilliance source and a simple instrument. The interpretation of the peak profiles measured is detailed using the well established formalism of small-angle scattering. The domain-size coarsening of the two ordered structures is studied and the interactions occurring between the dynamics of the two corresponding transitions are briefly discussed.

We discuss the conditions of the coherent scattering experiment in our case and we report preliminary measurements on one of our samples.

II. Description of the experiments

All experiments reported here have been done on the TROIKA (ID10) beam line at the ESRF (Grübel, Als-Nielsen & Freund, 1994).

Source

A high-intensity high-brilliance source is provided by the use of the third harmonic of an undulator. Slits 27 m from the source produce an effective source size of 0.21×0.21 mm.

Optics

The distance between the source and the sample is about 45 m. Monochromatization is achieved by means of an Si(220) crystal. An SiC mirror is used to limit harmonic contamination. The selected wavelength is 1.05 Å, just below the L_{III} absorption edge of Pt. The wavelength resolution $\Delta\lambda/\lambda$ is about 6×10^{-5}.

Collimation of the monochromatic beam

The high resolution is obtained by the use of pinholes of various diameters, produced by laser drilling of 50 μm-thick Pt sheets. These pinholes were developed for X-ray speckle experiments (Sutton *et al.*, 1991).

Two sets of pinholes have been used: one just before the sample (diameters 4 or 27 μm) for the incident-beam collimation and one for analysis of the scattered intensity (diameters 5, 20, 66 or 500 μm). The samples were placed at the centre of an Eulerian cradle, 8 cm after the first pinhole, and the second pinhole was placed on the 2θ arm of the diffractometer, 1.2 m from the sample, just before the detector. An incoming beam monitor was located just after the first pinhole.

Coherence of the beam

The transverse coherence length Λ of the beam at the sample is determined by the effective source size $A = 210$ μm at a distance $R = 45$ m (distance from the slits to the first pinhole).

$$\Lambda = \lambda R/2A = 11\,\mu\text{m}. \tag{1}$$

This means that the incident beam was fully coherent when collimation pinholes smaller than 11 μm were used. This can be verified from the results of Fig. 1. In this latter figure, the first aperture is 4 μm and the 5 μm pinhole has been used to scan across the beam. As the distance between the two pinholes was 1.4 m, the width of the diffraction was of the order of 40 μm, corresponding to an angle of 27 μrad and about 20 Fraunhofer fringes were observed.

The longitudinal coherence is given by

$$\lambda^2/2\delta\lambda = 0.87\,\mu\text{m}. \tag{2}$$

For coherent illumination of the sample, this must be larger than the optical path length difference:

$$\Delta L = 2L\sin^2\theta_B, \tag{3}$$

where L is the penetration length of the X-rays (15 μm here) and θ_B is the Bragg angle. For the (100) Bragg peak of Fe_3Al, ΔL is 1μm. One can consider that the condition is roughly fulfilled.

At the highest resolution used, the coherent scattering can be observed. We report some attempts to use this property at the end of this paper.

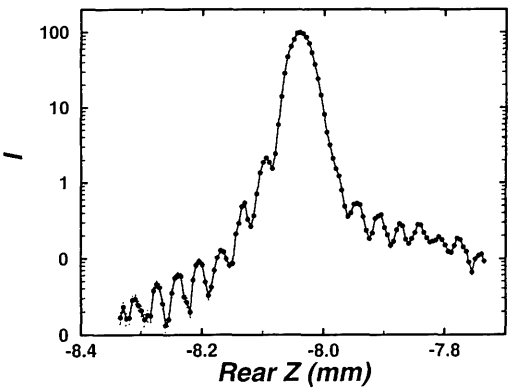

Fig. 1. Fraunhofer fringes with a 4 μm pinhole at 1.4 m from the detector: analysing aperture of 5 μm, the fringes are spaced 40 μm, *i.e.* 27 μrad.

Table 1. *Heat treatment of the samples studied in the experiment*

		B_2 (885 K)		
		0 s	100 s	1800 s
	DO_3			
	0 s		$M7$	
25.5 at.%Al	10 s	$M5$ (801 K)		
	100 s	$M'5$ (801 K)	$M'7$ (793 K)	
	1800 s			$M9$ (803 K)
24 at.%Al	B_2	$Q1$ 0 s	$Q'1$ 2 s (843 ±20 K)	$Q''1$ 200 s (890 K)

Samples and goniometry

Single crystals have been grown by the horizontal Bridgmann technique at Ecole des Mines de Saint-Etienne, France. The composition gradient in the height of the crystal is about 0.5%. The samples are slices about 100 μm thick, spark cut from single crystals and mechanically polished. The disordering annealings were made at about 120 K above the transition temperatures (1093 K for Fe–24 at.%Al and 1173 K for Fe–25.5 at.%Al). The samples were then quenched in a liquid-metal bath at room temperature. This treatment gives an initial state with the smallest possible domain size. The subsequent annealings were done in a molten-salt bath and are given in Table 1. For short times such as 2 s, the nominal temperature was not reached and the given temperature is the mean 'plateau' temperature. Successive states of the same sample are denoted as $'$ and $''$.

The single crystals were mounted on an Eulerian cradle with high precision of angular positioning (0.001°). They were cut with surfaces parallel to (100) planes. Experiments were done in symetrical reflection position in the horizontal plane. As only the (200), (100), (111) and $(\frac{1}{2}\frac{1}{2}\frac{1}{2})$ Bragg scattering peaks were studied, the diffraction angles were small enough to neglect beam-polarization effects.

Experimental resolution

In studying large-angle diffraction, the usual diffractometer equipment always has a direction of poor resolution in the reciprocal space (q space). For instance, for precise lattice-parameter determinations, only a very good resolution parallel to the **q** vector is necessary.

In the case of rapidly varying scattering intensity, either in diffuse scattering experiments (Huang scattering) or in peak-profile analysis for order domain size, strong experimental corrections are necessary, owing to the shape of the resolution volume in q space. This problem explains why peak-profile measurements are usually carried out by powder diffractometry (Poquette & Mikkola, 1969; Bley, Calvayrac & Fayard, 1974).

In the experiments reported here, a very good resolution is achieved in the three directions of the q space. For instance, with the 27 μm aperture before the sample and the 66 μm pinhole after the sample, one can roughly estimate the q resolution ($q = 4\pi \sin\theta/\lambda$, in Å^{-1}) close to a (100) Bragg position ($\theta_B \simeq 0.18$ rad) as:

4×10^{-4} Å^{-1} in the q direction;

$6 \times 10^{-}$ Å^{-1} along the vertical axis;

7×10^{-5} Å^{-1} along the second horizontal axis.

This means that it is possible to study domains a few thousand Å in size. Depending on the resolution needed, the set of pinholes has been changed in order that the experimental smearing is significantly smaller than the width of the peak profile. This is necessary because the intensities of the samples with the smallest domain sizes are fairly small. Fig. 2 shows typical results for a series of annealings of the same specimen. Owing to the very different domain sizes, the intensities are given on a logarithmic scale and the units are arbitrary (counts/monitor counts). Special attention has been paid to obtain precise data in the tail of the curves in order to discuss their asymptotic shape.

III. Methods of interpretation of the experiments

Theory

Warren (1969) has given a formalism for the broadening of Bragg superstructure peaks. He has mainly developed the case of $L1_2$ superstructure for the Cu_3Au alloy. In this alloy, four variants are present and the antiphase domain boundaries (APBs) are mainly of the first kind: they lie in a (100) plane with the antiphase vector in this plane. In such a case, no change of the order projected on a (001) axis of the crystal occurs when crossing an APB. Close to the corresponding (001) Bragg superstructure peak, the intensity has the shape of a flat disc and a sharp peak is observed along the [001] direction of the reciprocal lattice. Only in the perpendicular directions is observed the peak broadening corresponding to the finite size of the domains.

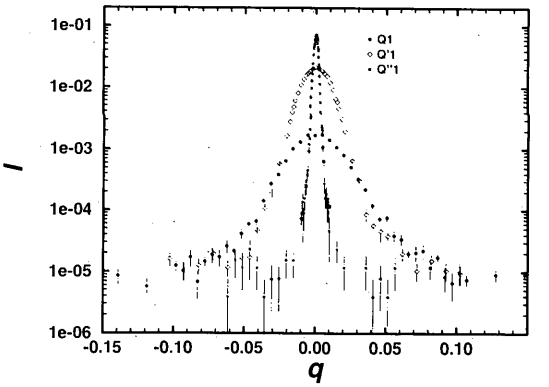

Fig. 2. Typical (100) peak profiles observed for the $Fe_{0.76}Al_{0.24}$ sample. Notice the large FWHM dynamic of the experimental set-up.

Moreover, if the domains are strongly faceted in the various (100) planes, the intensity has strong $1/q^2$ streaks along the [100] and [010] directions. This means that the isointensity figure should be a flat star and not a flat disc.

In our case, the intensity close to the superlattice point appears isotropic. For instance, for some experiments, the (100) and the (111) Bragg peaks have been measured. All the intensities have been studied along the direction of the Bragg vector. This provides a comparison of the changes of order when crossing an APB projected along the ⟨100⟩ and ⟨111⟩ directions in the lattice. Fig. 3 shows in the case of sample *M5* that the shapes of the two peaks are the same in the total intensity range. This isotropy is also confirmed by transmission-electron-microscopy observations.

Simplified model

We use the following assumptions, which have to be discussed:

(i) Each superstructure peak profile corresponds to the distribution of two variants of the ordered structure, separated by a unique kind of antiphase boundary.

(ii) There is no prefered orientation of the APB.

(iii) The APBs are gently curved.

(iv) The APBs are sharp.

(v) The fluctuations are neglected.

The occupation of the sites in the ordered crystal can be written as:

$$c(\mathbf{r}) = m(\mathbf{r}) \exp(-i\mathbf{G}_0 \cdot \mathbf{r}), \tag{4}$$

where $m(\mathbf{r}) = \pm\eta$ and η is the order parameter of the transition. As the intensities are not calibrated, the η temperature dependence can be neglected ($\eta \simeq 1$).

$\mathbf{G}_0$ is equal to $2\pi/d(100)$ in the case of the $A_2 \rightarrow B_2$ transition and to $G_0 = \pi/d(111)$ in the $B_2 \rightarrow D0_3$ transition. Only the (100) and the $(\frac{1}{2}\frac{1}{2}\frac{1}{2})$ Bragg positions are pertinent here. The other superstructure peaks are deduced from the lattice symmetry.

In both cases, crossing the APB corresponds to a sudden change of the sign of $m(\mathbf{r})$

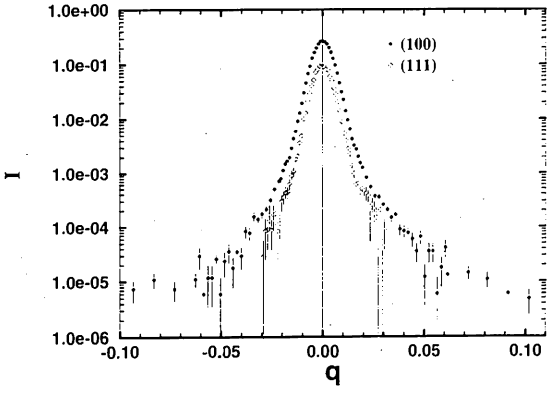

Fig. 3. Comparison of the (100) and the (111) scattering of sample *M5*; the peaks are shifted vertically to allow comparison of the profiles.

The intensity close to $\mathbf{G}_0$ is

$$I(\mathbf{K}) = \left| \int_v c(\mathbf{r}) \exp(i\mathbf{K} \cdot \mathbf{r}) \, \mathrm{d}^3\mathbf{r} \right|^2 = \left| \int_v m(\mathbf{r}) \exp[i(\mathbf{K} - \mathbf{G}_0) \cdot \mathbf{r}] \, \mathrm{d}^3\mathbf{r} \right|^2. \tag{5}$$

If $\mathbf{q} = \mathbf{K} - \mathbf{G}_0$ ($\mathbf{G}_0$ is chosen as a new origin), the usual formulation can be given:

$$I(\mathbf{q}) = \int_v \exp(i\mathbf{q} \cdot \mathbf{r})[m(\mathbf{r}) * m(-\mathbf{r})] \, \mathrm{d}^3\mathbf{r}, \tag{6}$$

where $*$ means a convolution product. In this calculation, v is the coherence volume, as defined by (1) and (2). If the sample is significantly larger than this volume, an average over the intensities scattered by various regions of the sample is observed. The reverse case is briefly discussed at the end of this paper.

Equation (4) is equivalent to the small-angle scattering of two interconnected phases each occupying half of the sample volume.

One can then transpose the small-angle techniques (Guinier & Fournet, 1955) and define:

a Guinier radius,

$$R_G = -3[\partial \ln I(\mathbf{q})/\partial q^2]; \tag{7}$$

and an integrated intensity,

$$\int I(\mathbf{q}) \, \mathrm{d}^3\mathbf{q} = \int_V m(\mathbf{r})^2 \, \mathrm{d}^3\mathbf{r} = V\eta^2. \tag{8}$$

Here V is the sample volume. The convolution product, in the case of sharp interfaces and assuming isotropy of the sample, can be written

$$m(\mathbf{r}) * m(-\mathbf{r}) \simeq \eta^2(V - S\mathbf{r} + \ldots). \tag{9}$$

S is the interface (APB) area in the sample. This gives Porod's law at large q values:

$$I(\mathbf{K}) \simeq (v\eta^2/\pi^2)(S/V)q^{-4} \tag{10}$$

and, without any calibration, the ratio V/S can give an estimation of the characteristic length:

$$\bar{l} = (V/S) = (4/\pi) \int q^2 I(\mathbf{q}) \, \mathrm{d}\mathbf{q} \Big/ \lim_{q \to \infty} q^4 I(\mathbf{q}). \tag{11}$$

The chord average length $\bar{l}$ (Méring & Tchoubar, 1968; Porod, 1982) has an unambiguous meaning in the case of percolated sytems, in contrast to the Guinier radius, which can be interpreted as a gyration radius only in dilute systems.

Experimental

The measurements of the intensity have been carried out on both sides of the maximum (see Fig. 3) along

Table 2. *Guinier (R_G) and Porod ($\bar{l}_p$) radii, in* Å, *of the studied samples: B_2 from* (100) *or* (111) *Bragg peaks, $D0_3$ from* ($\frac{1}{2}\frac{1}{2}\frac{1}{2}$) *Bragg peaks*

	B_2			$D0_3$		
Sample	t (s)	R_G	$\bar{l}_p$	t (s)	R_G	$\bar{l}_p$
$M5$	0	300 (5)	348 (20)	10	197 (4)	225 (20)
$M'5$	0	500 (7)	445 (15)	100	361 (5)	334 (30)
$M7$	100	960 (10)	870 (20)	0	10 (1)	–
$M'7$	100	881 (20)	720 (50)	100	146 (3)	208 (30)
$M9$	1800	4200 (500)	Electron microscopy	1800	710 (10)	790 (100)
$Q1$	0	78 (2)				
$Q'1$	2	130 (5)				
$Q''1$	200	800 (20)				

the q axis (*i.e.* θ–2θ scans). The Guinier radius has been obtained from a least-squares fit of the measured intensity within the half-maximum region. Fig. 4 shows a $\ln(I)$ *vs* q^2 plot (q positive or negative), classical in small-angle scattering. It is verified that the intensity in the central region is almost Gaussian, as assumed in the Guinier approach. In the figure, the Gaussian fit appears as a straight line at the top of the curve. Another length estimation can be obtained from the full width at half-maximum of the profile (Debye–Scherrer method). The results are the same since the central part of the curve is assumed to be Gaussian.

The resolution of the experiment (ε) has been measured by means of a well aged sample ($M9$ in Table 1) using the (100) peak. The Guinier radius has been corrected by the usual formula:

$$R_{\text{corr}}^{-2} = R_{\text{fit}}^{-2} - \varepsilon^2. \qquad (12)$$

This formula assumes classical convolutions between Gaussian curves. The resolution varies when the pinholes are changed. The main correction arises when the 500 µm pinhole after the sample is used: $\varepsilon = 7 \times 10^{-4}$ Å^{-1}. Some measurements have been carried out with two pinholes in order to increase the counting rate in the tails of the curves. This gives a better precision in the determination of the Porod asymptotic limit. It has been verified that the corrected R_G are independent of the resolution. This provides some tests of the validity of the approximations used. The corrections were in all cases less than 25%.

The corrected R_G are given in Table 2. However, from Fig. 4, the intensity is obviously not Gaussian at levels lower than 30% of the maximum.

Fig. 5 shows a plot of Iq^4 *vs* q for the same sample as in Fig. 4. The plot has the classical shape of a Porod plot in small-angle scattering experiments (Porod, 1982): after some oscillations, a roughly constant limit is reached. This is the Porod limit (the arrows in Fig. 5 correspond to $qR_G = 4.5$). In practice, this limit has been calculated by a least-squares fit in the region of q where $4.5 < qR_G < 10$. A small background correction has been necessary due to the noise of the detector, ≤ 0.06 counts s^{-1}, but the results, given in Table 2, are far less precise than R_G.

IV. Results and discussion

Size increase and diffusion constant

Table 2 summarizes the results obtained. In all experiments where reasonable estimations of the Porod behaviour can be given, the value of $\bar{l}$ is close to the Guinier radius. One can then consider that R_G is

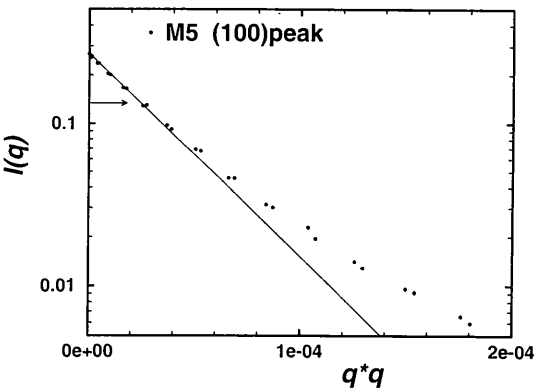

Fig. 4. Guinier plot close to the (100) superstructure peak (sample $M5$: $R_G = 300$ Å).

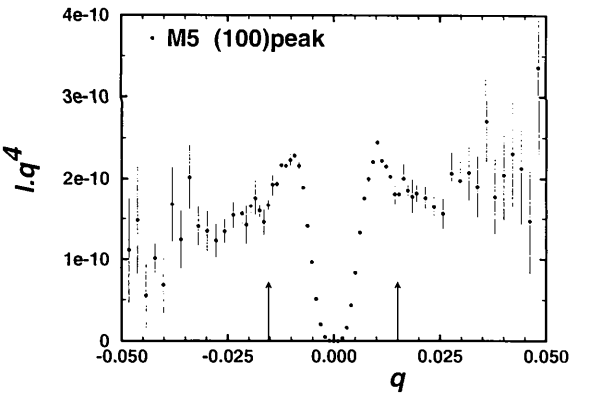

Fig. 5. Porod plot for the same sample as in Fig. 4: Iq^4 *vs* q.

a reliable estimate of the characteristic length of the percolated sytem. It is thus assumed in the following that $\bar{l} = R_G$. Contrary to small-angle experiments on percolated systems [FeCr (Bley, 1992)], no correlations appear between the opposite phases. In the system studied here, no long-range diffusion is necessary to increase $\bar{l}$ and no depleted zones appear in the vicinity of a phase. This depleted zone explains the repulsion between like phases revealed by the strongly oscillating small-angle intensity observed in the decomposition of alloys. On the other hand, a $t^{1/3}$ behaviour is generally considered as a normal size increase of precipitates in unmixing alloys (Livet & Bloch, 1985).

Here, one assumes that the usual behaviour of non-conservative systems is valid:

$$\bar{l} = [D(c,T)t]^{1/2}. \qquad (13)$$

The apparent diffusion constant D is temperature and concentration dependent. We use R_G for the calculation of D. From the results of Table 2, D can be estimated for the two transitions studied. For the $A_2 \rightarrow B_2$ transition (ageing at 885 or 890 K), two significantly different values are obtained:

$D = 8.9\,(1) \times 10^{-17}\,\mathrm{m^2\,s^{-1}}$ for the 25.5 at.% concentration;

$D = 3.2\,(1) \times 10^{-17}\,\mathrm{m^2\,s^{-1}}$ for the 24 at.% concentration.

This difference cannot be explained by the heat-treatment temperature variations. The second sample is closest to the $A_2 \rightarrow B_2$ transition line. If the driving force for the time evolution given in (13) is the surface free energy, D should decrease close to a second-order transition line. This simple scheme has been contested (Allen & Cahn, 1979).

Some uncertainty is borne here by the concentration gradient occurring in our samples: a 1% concentration difference leads to a 75 K change of transition temperature. With such a sensitivity, the state of the system after quenching is difficult to reproduce. This can explain the observed decrease of the size of the B_2 domains between the $M7$ and the $M'7$ samples, though this decrease may be related to the following discussion.

Interaction between the two transitions

For the $B_2 \rightarrow D0_3$ transition, strong differences are observed between the $M5$–$M'5$ and the $M'7$–$M9$ heat treatments:

$D = 1.00\,(5) \times 10^{-17}\,\mathrm{m^2\,s^{-1}}$ if the B_2 phase is not developed;

$D = 0.21\,(1) \times 10^{-17}\,\mathrm{m^2\,s^{-1}}$ if the sample has been aged in the B_2 phase.

The explanation of this result can be found in the difference between the diffusion paths. If the $D0_3$ domains grow among large B_2 domains, a second-neighbour complex diffusion process must occur. One then observes a strong decrease of the apparent D.

The fluctuations

For the $D0_3$ transition, the heat-treatment temperature is not too far from the critical temperature in the case of the 25.5 at.% composition, $\theta \simeq \Delta T/T_c \simeq 0.03$ and the width of the antiphase boundaries is of the order of the correlation length $\xi \simeq 2.5\theta^{-\nu} \simeq 25$ Å. The constant 2.5 Å is the first-neighbour distance and roughly corresponds to the unit scale length, and $\nu \simeq 0.63$ is the usual critical exponent. To check how ξ interacts with the Porod behaviour, we have superimposed in Fig. 6 the experimental points of the $M5$ sample using a curve corresponding to Porod's law and another corresponding to an estimation of the fluctuations. It is clear from this figure that the fluctuations can be neglected in the Porod-limit determination.

The elastic interactions

In alloys, the elastic interactions are responsible for phonon and displacement ('Huang') scattering. We discuss here briefly why these are not observed.

The phonon and Huang scattering both have a q^{-2} behaviour. In the case considered, the experiments are carried out at room temperature and results are obtained from the first Bragg peaks. Integrated in the first Brillouin zone, the Bragg intensity is dominant. It is assumed, however, that both contributions are of the same order of magnitude. The Bragg intensity is roughly $1/(\bar{l}q^4)$ for $q \gg 1/\bar{l}$ and the phonon-Huang scattering is $1/q_{ZB}q^2$, where q_{ZB} is the size of the Brillouin zone, approximately π/a. The crossover between the two behaviours occurs at $q_1 = (\pi/a\bar{l})^{1/2}$. This crossover decreases towards low q at a slower rate than $q^2 = 3/\bar{l}$, the region where the Porod behaviour becomes dominant. For instance, if $\bar{l} = 100$ Å, the ratio between the two crossovers q_1/q_2 is close to 3, throwing the phonon-Huang contribution out of the q region where Porod analysis is performed.

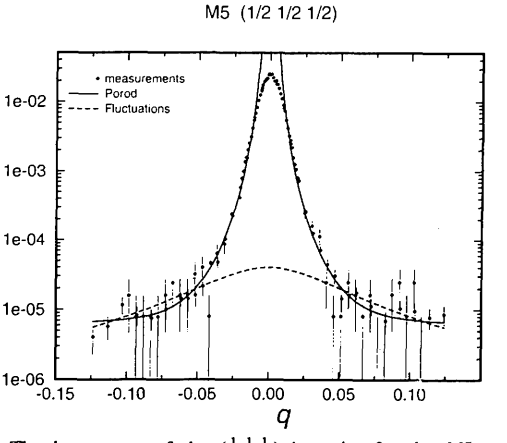

Fig. 6. The lower part of the $(\frac{1}{2}\frac{1}{2}\frac{1}{2})$ intensity for the $M5$ sample. The Porod term is compared with the diffuse scattering estimation ($\xi = 25$ Å).

Scaling of the peak profiles

In order to discuss the size distribution of the domains, the spectra have been plotted in a renormalized form in Fig. 7. The intensities have been divided by their maximum values and qR_G gives the units of the horizontal axis. All curves are about the same for intensities larger than a few per cent of the maximum. At lower values, some discrepancies appear, but the strongest differences appear here between different pinholes on the same Bragg peak. Though in all results given the experimental smearing is small [less than 20% in (12)], the change of shape in the asymptotic region is great. Obviously, this is due to the poor resolution of the measurements in the asymptotic region. As we worked with point detectors, the only way to increase statistics in this part of the curves was to use larger pinholes. Further treatments (Fourier transform, size-distribution functions *etc.*) depend on the asymptotic part of the curves and must therefore use deconvolution techniques.

Similar shapes are observed between the various (100) peak profiles. This means that the time evolution of the system can be characterized with a unique length scale, which represents the distance between type 1 APBs separating the two interconnected B_2 variants.

The similarity with the $(\frac{1}{2}\frac{1}{2}\frac{1}{2})$ peak profiles has to be discussed. In the case of greatly different sizes of $B_2/D0_3$ domains, the simplified model given can be applied: only two $D0_3$ variants in large B_2 domains ($M'7$ sample). This approximation is not valid in the case of the $M'5$ sample: the B_2 domains have the same extension as the $D0_3$ domains and the four $D0_3$ variants contribute to the intensity profile. There is, nevertheless, no measurable difference in the shape of the peak profiles.

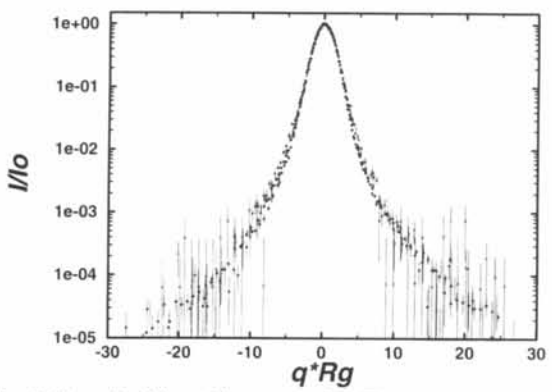

Fig. 7. Normalized intensities *versus* qR_G. The measured peak profiles have the same form: • (100) for sample $M5$, 500 μm aperture; □ (0.5 0.5 0.5) for sample $M5$, 500 μm aperture; ♦ (100) for sample $M7$, 500 μm aperture; ▲ (100) for sample $M7$, 66 μm aperture; + (100) for sample $M'5$, 500 μm aperture; * (100) for sample $M'5$, 66 μm aperture.

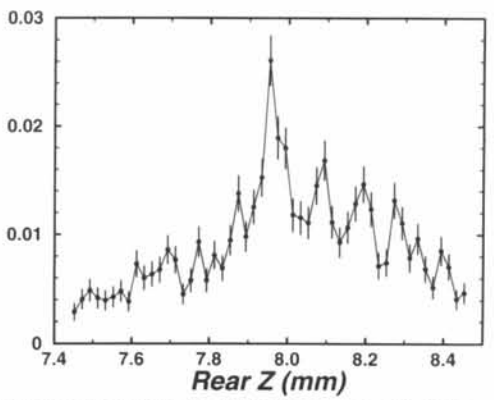

Fig. 8. Typical 'speckle' profile: the (100) Bragg peak of the $Q''1$ sample (24 at.%, aged 200 s at 990 K).

V. Coherent scattering

In the usual X-ray diffraction experiments, the sample is much larger than the coherence length of the beam. In such a case, the intensity observed in a typical experiment (for instance in Fig. 2) is an average over the intensities diffracted by the various parts of the sample. If the beam is coherent, the amplitude due to the whole sample interferes. Fig. 8 shows the resulting profile measured on the (100) Bragg peak of the $Q''1$ sample. The smallest pinholes have been used.

This profile is qualitatively similar to a speckle diffraction pattern (Grübel, Als-Nielsen, Abernathy *et al.*, 1994). The typical pseudo-period of the 'noise' is 40 μm, corresponding to the 27 μrad period of the Fraunhofer fringe pattern and the error bars show that this noise is significantly larger than the statistical errors. A simple theory can give the typical distribution of the speckle noise around an 'average curve' (*i.e.* curves like Fig. 2 or Fig. 6) if the beam is fully coherent. The measured intensity is the square modulus of the

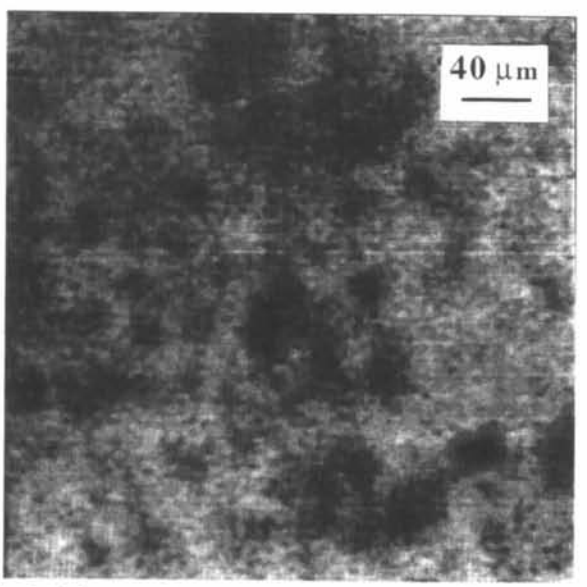

Fig. 9. Hologram of the ordered B_2 domains in the $Q''1$ sample from the (100) Bragg peak.

amplitude of the Fourier transform of $m(\mathbf{r})$. One can consider that the two components of the complex amplitude have Gaussian distributions. In this case, the intensity distribution $p(I)$ can be written

$$p(I) = (I/\langle I\rangle)\exp(-I/\langle I\rangle).$$

This is equivalent to the theory of Gaussian light (Siegert, 1943; Jakeman & Pike, 1968). In this case, the second-order normalized cumulant of the intensity is 1. This is obviously not the case in Fig. 8. The results given are too partial to carry out a quantitative analysis, but the main explanation may be the poor achievement of the longitudinal coherence conditions in this experiment [see (2) and (3)]. Much work has however to be done in order to obtain a better understanding of all the parasitic effects of this type of experiment. This short discussion can also be illustrated by the photograph given in Fig. 9. Diffuse speckles can be observed on the 40 μm scale (same sample). This photograph is a hologram of the domains of the sample.

VI. Concluding remarks

This preliminary experiment shows that synchrotron radiation gives a new insight in the study of phase transitions.

Close to Bragg peaks, large domain sizes can be studied. The small-angle techniques can be used for the interpretation of the experiments. In the case studied, the dynamics of the domain growth of the DO_3 phase shows marked differences between large and small B_2 domains. Changes in the growth kinetics of B_2 domains are observed, related to the proximity of the critical line. This problem has to be dealt with from *in situ* dynamical studies of ordering.

The high brilliance of the sources gives the possibility of obtaining coherent X-ray beams. A lot of holographic X-ray techniques will now appear. This introduces new techniques for the study of strongly fluctuating systems (Sutton *et al.*, 1991).

This experiment has been made possible by the help of the team of Mark Sutton and Brian Stephenson. We have benefited from the pioneering work of this team. We have used their pinholes and other experimental accessories, and we owe them a great debt for experimental help.

References

ALLEN, S. M. & CAHN, J. W. (1975). *Acta Metall.* **23**, 1017–1026.
ALLEN, S. M. & CAHN, J. W. (1976). *Acta Metall.* **24**, 425–437.
ALLEN, S. M. & CAHN, J. W. (1979). *Acta Metall.* **27**, 1085–1095.
ANTHONY, L. & FULTZ, B. (1989). *J. Mater. Res.* **4**, 1140–1142.
BLEY, F. (1992). *Acta Metall. Mater.* **40**, 1505–1517.
BLEY, F., CALVAYRAC, Y. & FAYARD, M. (1974). *J. Appl. Cryst.* **7**, 493–497.
CHEARY, R. W. & GRIMES, N. W. (1972). *Acta Cryst.* A**28**, 454–458.
ENGLISH, A. T. (1966). *Trans. Am. Inst. Min. Metall. Pet. Eng.* **236**, 14.
GRÜBEL, G., ALS-NIELSEN, J., ABERNATHY, D., VIGNAUD, G., BRAUER, S., STEPHENSON, G. B., MOCHRIE, S. G. J., SUTTON, M., ROBINSON, I. K., FLEMING, R., PINDAK, R., DIERKER, S. & LEGRAND, J. F. (1994). *ESRF Newsletter*, **20**, 14–15.
GRÜBEL, G., ALS-NIELSEN, J. & FREUND, A. K. (1994). *J. Phys. (Paris) IV Colloq.* **9**, 27–34.
GUINIER, A. & FOURNET, G. (1955). *Small-Angle Scattering of X-rays.* New York: Wiley.
HOHENBERG, P. C. & HALPERIN, B. I. (1977). *Rev. Mod. Phys.* **49**, 435–479.
INDEN, G. & PEPPERHOFF, W. (1990). *Z. Metallkd.* **81**, 770–773.
JAKEMAN, E. & PIKE, E. R. (1968). *J. Phys. A: Gen. Phys.* **1**, 128–138.
KÖSTER, W. & GÖDECKE, T. (1980). *Z. Metallkd.* **71**, 765–769.
KUBASCHEWSKI, O. (1982). *Iron – Binary Phase Diagrams.* Berlin: Springer-Verlag.
LIVET, F. & BLOCH, D. (1985). *Scr. Metall.* **19**, 1147–1151.
MÉRING, J. & TCHOUBAR, D. (1968). *J. Appl. Cryst.* **1**, 153–165.
MORGAND, P., MOUTURAT, P. & SAINFORT, G. (1968). *Acta Metall.* **16**, 867–875.
OKAMOTO, H. & BECK, P. A. (1971). *Metall. Trans.* **2**, 569–574.
OKI, K., HASAKA, M. & EGUCHI, T. (1973). *Jpn. J. Appl. Phys.* **12**, 1522–1530.
PARK, B., STEPHENSON, G. B., LUDWIG, K. F. JR & ALLEN, S. M. (1992). *Mater. Res. Soc. Symp. Proc.* **205**, 119.
POQUETTE, G. E. & MIKKOLA, D. E. (1969). *Trans. Am. Inst. Min. Metall. Pet. Eng.* **245**, 743–751.
POROD, G. (1982). *Small-Angle X-ray Scattering*, edited by O. GLATTER & O. KRATKY, pp. 17–51. London: Academic Press.
RIMLINGER, L. (1971). *C. R. Acad. Sci. Ser. C*, **272**, 22.
SIEGERT, A. J. F. (1943). MIT Radiat. Lab. Rep. No. 465. MIT, Cambridge, MA, USA.
SUTTON, M., MOCHRIE, S. G. J., GREYTAK, T., NAGLER, S. E., BERMAN, L. E., HELD, G. A. & STEPHENSON, G. B. (1991). *Nature (London)*, **352**, 608–610.
SWANN, P. R., DUFF, W. R. & FISHER, R. M. (1972). *Metall. Trans.* **3**, 409–419.
TAYLOR, A. & JONES, R. M. (1958). *J. Phys. Chem. Solids*, **6**, 16–37.
WARREN, B. E. (1969). *X-ray Diffraction.* Reading, MA: Addison-Wesley.